

Origin of surface segregation in LiCoO₂: A DFT+*U* studyA. O. Boev ¹, M. Yu. Arsentev ², S. S. Fedotov ¹, A. M. Abakumov ¹ and D. A. Aksyonov ¹¹Skolkovo Institute of Science and Technology, 121205 Moscow, Russian Federation²Infochemistry Scientific Center (ISC), ITMO University, 9 Lomonosova Street, St. Petersburg 191002, Russia

(Received 14 November 2023; revised 29 March 2024; accepted 10 April 2024; published 13 May 2024)

In recent years, surface segregation of doping elements in layered oxide positive electrode (cathode) materials for metal-ion batteries has drawn considerable attention. It was repeatedly shown that an increase of surface concentration of a particular element can have either detrimental or beneficial impact on the stability of the electrochemically active surface, manifesting declined or improved electrochemical performance. However, the physical and chemical reasons for segregation remain poorly understood. To explain the behavior of commercially important doping elements, such as Mg, Al, Ti, V, Cr, Mn, Fe, and Ni, we performed a density functional theory study of their segregation at the (104) low-energy surface of LiCoO₂. By careful control of local oxidation states and magnetic moments of surface atoms, we find their most stable configurations. We discover that all elements, except Al and Cr, are prone to segregation that is primarily driven by the surface energies' difference between the host and solute lattices, which is explained through crystal-field stabilization energies. An additional contribution to segregation is caused by the elastic energy penalty to the ionic size mismatch effect. Finally, we rationalize the available experimental results and provide several predictions of highly segregating and nonsegregating dopants.

DOI: [10.1103/PhysRevMaterials.8.055403](https://doi.org/10.1103/PhysRevMaterials.8.055403)

I. INTRODUCTION

Layered oxides of 3*d* metals, commercially used as cathodes in Li-ion batteries [1–4], are prone to oxygen loss and surface reconstruction. Poor ionic conductivity of a reconstructed thin surface layer results in the growth of interfacial resistance [5–7], resulting in electrochemical performance degradation. The driving force for surface reconstruction is the loss of oxygen itself; however, an additional contribution can be provided by the easier formation of surface antisite defects [8,9] when the transition metals migrate inside the Li sites [5,6,10–12].

One of the promising ways to minimize this adverse effect is to dope a cathode material with strongly segregating elements that can improve surface stability [13–15]. The stabilization is due to the surface energy decrease (thermodynamic stabilization), oxygen release retention, penalizing formation of antisite defects, and increasing dopants' migration barriers into Li sites (kinetic stabilization). The improvement of the layered oxides' electrochemical performance as a result of surface segregation has been repeatedly reported for different layered oxides: Ti in LiCoO₂ [16], Ti in NaMnO₂ [17], Sb in LiNiO₂ [14], and others. On the other hand, negative effects of segregation were also reported, such as for Ni in Li- and Mn-rich oxides [18] and Ni/Co in Li- and Mn-rich oxides [19]. Studies by Li *et al.* [20], Wang *et al.* [21], and others have confirmed the presence of segregation either by x-ray photoelectron spectroscopy (XPS) or electron energy loss spectroscopy (EELS) mapping, but it remains a difficult task since the effect is restricted to several atomic layers. It is also difficult to prove unequivocally that the observed improvement/deterioration is caused by surface segregation, thus calling for a better understanding of the segregation phenomenon.

In this case, computational studies that have relied on density functional theory (DFT) may append the missing experimental information. For example, the DFT-PBE (PBE is a flavor of the exchange-correlation functional by Perdew-Burke-Ernzerhof) study of Ni-rich LiNi_xMn_yCo_zO₂ (NMC) confirmed Ni segregation and Ni-Li surface antisite favorable formation [8]. On the other hand, Shin *et al.*, using DFT-PBE, performed screening of dopants for Li₂MnO₃ and identified Os, Sb, Ru, Ir, and Ta as highly segregating elements that decrease oxygen release [22].

Despite the shown importance of segregation, it remains poorly understood why particular elements do segregate and others are not. Dahl *et al.*, by considering the segregation of di-, tri-, and tetravalent metals in LiCoO₂ (LCO), found that the driving force for segregation enhances with the increase of the dopant ionic radius [23]. However, in their study, most of the critical transition metals, such as Ni and Mn, were not considered and the electronic structure effects are missing due to the empirical nature of the Coulomb-Buckingham potentials that were used.

To fill this gap, we consider surface segregation in LCO for a pragmatical set of solutes (dopants) using DFT calculations. The choice of solutes is mostly governed by their significance in commercial applications and available experimental data on segregation. In particular, the surface concentration enhancement for Ti [15,20,21], Ni [24], and Mg [25] was experimentally reported in single-doped and co-doped LCO, while no segregation was found for Al [26]. Cr and Fe are known to form solid solutions in LCO [27,28], but their presence on a surface is unknown. Finally, V is known to be insoluble in LCO, but, according to the results of empirical modeling [23], it should demonstrate very strong segregation, which can stabilize its solution in surface layers.

In Sec. II, we continue with the description of the calculation details. In Sec. III A, we report on solution energies for the considered elements in the bulk LCO; in Sec. III B, we discuss the electrochemically active (104) surface; and in Sec. III C, the results of surface segregation are provided and the origin of segregation is revealed. In Sec. IV, the alignment of the obtained computational results with the available experimental data is discussed. The conclusion is given in Sec. V.

II. COMPUTATIONAL DETAILS

Density functional theory (DFT) calculations are performed using the Perdew-Burke-Ernzerhof (PBE) flavor [29] of the generalized gradient approximation (GGA) to the exchange-correlation functional and standard projected-augmented wave (PAW) potentials as implemented in the VASP program [30]. To take into account the strongly correlated character of the d electrons, a Hubbard-like correction is added within the Dudarev scheme [31]. The U values are collected in Table S1 (see the Supplemental Material [32]). The impact of the U values on the segregation energies is detailed in Sec. S7.4 in the Supplemental Material [32] (see, also, Refs. [9,33–43] therein). The energy cutoff is 400 eV, the k -point spacing is less than 0.3 \AA^{-1} , and the maximum force acting on each atom after relaxation is less than 0.05 eV/\AA . In particular, our convergence tests, provided in Table S24 in the Supplemental Material [32], show that the $1 \times 1 \times 1$ k -point mesh is enough for a 224-atom slab to achieve sufficient accuracy of the segregation energies (maximum error less than 0.1 eV and qualitative agreement). For slab calculations, only one k point normal to the surface is used. To minimize the periodic interactions between the doping elements, we use a 128-atom bulk supercell and 224-atom (104) slabs of LiCoO_2 with a 15 \AA vacuum region in our calculations (see more size convergence details in Sec. S7.1 in the Supplemental Material [32]). To guarantee accurate alignment of the Fermi energy, a dipole correction is applied normal to the surface [44]. The occupation matrix control (OMC) scheme [45] is used to stabilize the orbital order of the transition elements and robust localization of small polarons. The van der Waals correction was observed to have an influence on segregation energies of less than 0.1 eV (further details can be found in Sec. S7.3 in the Supplemental Material [32] and Refs. [34,37,41,46–51] therein). All the calculations are performed using the SIMAN software package [52].

Model-based solution energies of M in bulk LiCoO_2 with respect to E_{LiMO_2} are calculated as

$$E_s = E_{\text{tot}} - (n - 1)E_{\text{LiCoO}_2} - E_{\text{LiMO}_2}, \quad (1)$$

where E_{tot} is the total energy of an ideal 128-atom supercell with composition $(n - 1)\text{LiCoO}_2\text{-LiMO}_2$ ($n = 32$, size test is provided in Table S22 in the Supplemental Material [32]), E_{LiCoO_2} is the total energy per formula unit of bulk LiCoO_2 , and E_{LiMO_2} is the total energy per formula unit of bulk LiMO_2 in its most stable polymorphic phase, as reported by the Materials Project [53], or fully optimized $R\bar{3}m$ phase. Since the LiMgO_2 compound is incompatible with the highest possible oxidation state of Mg, the solution energy for Mg is calculated relative to $\text{MgO} + 1/2\text{Li}_2\text{O}_2$ or $\text{MgO} + 1/2\text{Li}_2\text{O} + 3/4\text{O}_2$.

The binding energy between the solute and additional small hole polaron (AP) is calculated as

$$E_b = E^{\text{M+AP}}(3\text{NN}) - E^{\text{M+AP}}(1\text{NN}), \quad (2)$$

where $E^{\text{M+AP}}$ is the total energy of the bulk supercell containing a complex of $\text{M}^{2+/4+}$ solute and $\text{Co}^{4+/2+}$ in the first nearest-neighbor (1NN) or third nearest-neighbor (3NN) position.

The surface energy of a slab with the (104) surface is calculated as

$$\gamma = \frac{E_{\text{slab}} - E_{\text{bulk}}}{2A}, \quad (3)$$

where E_{slab} is the total energy of the slab with a surface, E_{bulk} is the total energy of bulk LiCoO_2 with the same number of formula units, and A is the surface area.

Segregation energies of M in substitution positions at the (104) surface are calculated as

$$E_{\text{seg}} = E_{\text{slab}}^{\text{M}} - E_{\text{slab}} - dE^{\text{M}}, \quad (4)$$

where $E_{\text{slab}}^{\text{M}}$ is the total energy of the slab with M in the surface transition metal (TM) position, E_{slab} is the total energy of the ideal (104) slab, and $dE^{\text{M}} = E_{\text{LiCo}_{1-x}\text{M}_x\text{O}_2} - E_{\text{LiCoO}_2}$ (see Fig. S1 in the Supplemental Material [32]).

In our analysis, we refer to the relative ionic size defined as a ratio of solute and host Shannon ionic radii [54],

$$\delta R = R_{\text{sol}}/R_{\text{Co}^{3+}\text{LS}}. \quad (5)$$

To estimate the ionic size mismatch effect, we separate segregation energy into elastic $E_{\text{seg}}^{\text{elastic}}$ and chemical $E_{\text{seg}}^{\text{chem}}$ contributions. The elastic contribution is calculated using modified structures, where the doping element has been substituted back with Co (Co_M) without ionic relaxation [55,56] (see more details of the methodology in Sec. S5.1 in the Supplemental Material [32]) as

$$E_{\text{seg}}^{\text{elastic}} = E_{\text{slab}}^{\text{Co}_M} - E_{\text{slab}} - dE^{\text{Co}_M}. \quad (6)$$

The chemical contribution is calculated as a difference between the segregation energy and the elastic contribution,

$$E_{\text{seg}}^{\text{chem}} = E_{\text{seg}} - E_{\text{seg}}^{\text{elastic}}. \quad (7)$$

One drawback of the $E_{\text{seg}}^{\text{elastic}}$ definition is that it consists of two parts itself: the first part is due to the deformation of the surrounding lattice, which is produced by solute, while the second part is caused by the distorted $\text{Co}_M\text{-O}$ bonds (Table S13 in the Supplemental Material [32]), which is completely artificial. The second part can be fully compensated only if disturbances caused by the solute are equivalent in the bulk and at the surface, which is hardly achieved in real cases. Otherwise, the compensation is incomplete, causing (over/under)estimation of the elastic contribution.

Therefore, $E_{\text{seg}}^{\text{elastic}}$ is just a useful instrument to rationalize the segregation energy, but it does not allow one to separate the segregation energy into elastic and chemical contributions in a strict sense.

TABLE I. Calculated solution energies E_s (SG) in eV of dopants M for Co-substitution positions in LiCoO₂ ($R\bar{3}m$) relative to the lowest-energy LiMO₂ phase with the space group (SG) [Eq. (1)]. The E_s ($R\bar{3}m$) is calculated relative to the metastable LiMO₂ ($R\bar{3}m$) phase. The local magnetic moments of the dopant and Co atom with the additional polaron, M-O distances in Å, and Co³⁺/Mⁿ ionic radii ratio δR [Eq. (5)] are also provided. The experimentally observed solubility limit x is given as a maximum concentration of M in a single-phase LiCo_{1-x}M_xO₂ compound.

Configuration	M-O	SG	μ_B (M)	μ_B (AP)	E_s (SG)	E_s ($R\bar{3}m$)	δR	x
Co ³⁺ LS	1.94×6	$R\bar{3}m$	0				1.00	
Co ²⁺ HS	2.06×6		2.68				1.36	
Co ⁴⁺ LS	$1.99 \times 2, 2.00 \times 4$		1.03				0.96	
Mg ²⁺ + AP(Co ⁴⁺) INN	$2.02 \times 2, 2.03 \times 2, 2.06 \times 2$	^a	0	1.02	0.08	-0.78	1.32	0.1 [57], 0.5 [58]
Al ³⁺	1.93×6	$P4_12_12$	0		0.01	-0.07	0.98	0.6–0.8 [26,59,60]
Ti ⁴⁺ + AP(Co ²⁺) INN	$1.94 \times 2, 1.99 \times 2, 2.03 \times 2$	$I4_1/amd$	0.01	2.68	-0.47	-0.56	1.11	0.1 [61], 0.2 [62]
V ⁴⁺ + AP(Co ²⁺) INN	$1.91 \times 2, 1.99 \times 2, 2.00 \times 2$	$R\bar{3}m$	1.03	2.68	0.39	0.39	1.06	
Cr ³⁺ HS	2.00×6	$R\bar{3}m$	2.96		0.10	0.10	1.13	1.0 [27]
Mn ³⁺ HS	$1.93 \times 2, 2.06 \times 4$	$C2/m$	3.82		0.38	0.22	1.18	0.2 [63,64]
Fe ³⁺ HS	2.01×6	$Pm\bar{m}n$	4.24		0.14	0.06	1.18	0.2 [65], 0.25 [28]
Ni ³⁺ LS	$1.94 \times 4, 2.04 \times 2$	$P2/c$	1.29		0.06	-0.01	1.03	1.00 [66,67]

^aMgO ($Fm\bar{3}m$) + 0.5Li₂O₂ ($P6_3/mmc$) combination of phases is used.

III. RESULTS

A. Bulk solubility

We start by considering ideal solid solutions of Mg, Al, Ti, V, Cr, Mn, Fe, and Ni in bulk LiCoO₂ (LCO) with $R\bar{3}m$ symmetry and study the orbital order of solutes and their solution energies, with E_s defined as a substitution energy of Co for M relative to the LiMO₂ phase [Eq. (1)]. The solution energies that are provided are model based, assuming that the most stable phase within LiCoO₂ during synthesis is LiMO₂, which is expected to be the case for Al, Ni, Mn, Fe, and Cr. However, establishing this assumption rigorously, particularly for Mg, V, and Ti, would necessitate the construction of quaternary phase diagrams. As this is beyond the scope of our current objectives, any correlation drawn between our calculated solution energies (E_s) and experimental solubilities should be considered conjectural.

To find the most stable electronic configuration of the solutes, we consider all reasonable oxidation and spin states for solutes and neighboring Co atoms, which are compiled in Table S1 in the Supplemental Material [32]. The calculated solution energies, local magnetic moments, and M-O distances of dopants in LCO for the most stable and all configurations are collected in Table I and in Table S2 (see Supplemental Material [32]), respectively.

The Co³⁺ in bulk LCO prefers a low-spin (LS) state with zero local magnetic moment. Its substitution with trivalent elements, such as Al, causes only a slight variation of interatomic distances around it, while the oxidation and spin states of the neighboring Co remain unchanged. The same is true for Ni, Mn, Cr, and Fe, which prefer to stay in the +3 state. Here, Mn, Cr, and Fe are in high spin, while Ni is in the low-spin state. The aliovalent substitution with divalent Mg leads to the formation of an additional small hole polaron (AP) (Co⁴⁺) at the INN position relative to the solute atom on the TM sublattice. In turn, the substitution with V and Ti shows that they behave as tetravalent elements and prefer the 4+ oxidation state, leaving behind the additional small electron polaron (Co²⁺) also at the INN position. The formation of APs is

required to maintain the charge balance. The formed M-AP defects have 0.32, 0.42, and 0.21 eV binding energies [Eq. (2)] for Ti, V, and Mg, respectively. We also tried to obtain the V⁵⁺ state, but it turned out to be unstable and decomposes into V⁴⁺+2AP(Co²⁺) (see Table S2 in the Supplemental Material [32]).

The calculated solution energies of dopants E_s are in good overall agreement with the experimentally observed solubilities (see more details in Sec. IV). The well-dissolving trivalent elements, such as Al, Cr, Fe, and Ni, have slightly positive E_s lying within the 0.01–0.14 eV range, which is sufficiently small for the entropy-driven formation of solid solutions [68]. For Al, Cr, and Ni, the solution energy grows almost linearly with the increase of the dopant's ionic radii (Fig. 1). Surprisingly, Mn has moderately large E_s of 0.4 eV, which is, at first sight, inconsistent with the formation of LiMn_{0.2}Co_{0.8}O₂ solid solutions [63,64]. Apparently, the Mn-Mn interactions are responsible for its stabilization at $x = 0.2$, while our E_s is obtained in the limit of low concentrations.

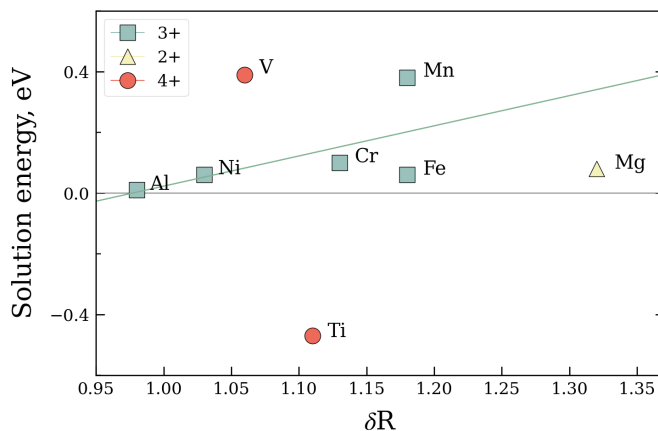


FIG. 1. Solution energies of considered dopants in LCO as a function of ionic radii ratio [Eq. (5)]. Elements with different oxidation states in LCO are shown with different colors. Pearson correlation coefficient for 3+ elements is 0.611.

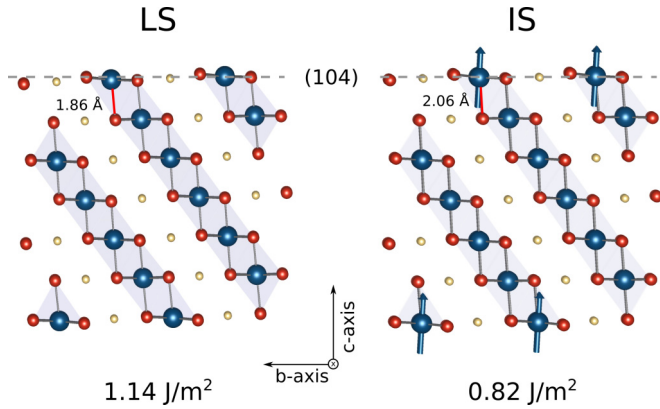


FIG. 2. Atomic and magnetic structure of the (104) LCO surface with LS and IS Co^{3+} ions. Surface energies and M-O distances are also shown.

Another explanation is that experimentally synthesized $\text{LiMn}_x\text{Co}_{1-x}\text{O}_2$ ($x \leq 0.2$) are LCO- Li_2MnO_3 nanodomain mixtures, which are hardly distinguishable by powder x-ray diffraction (XRD) from the true solid solution [69].

The divalent Mg has a slightly positive E_s , which also agrees with its good solubility in bulk both at the Li and Co positions ($\text{Mg}_{\text{Li}}^+ + \text{AP}(\text{Co}^{2+})$ and $\text{Mg}_{\text{Co}}^- + \text{AP}(\text{Co}^{4+})$ configurations given in Table S2 in the Supplemental Material [32]).

The tetravalent Ti has moderately negative E_s (-0.5 eV), which is in agreement with the experimentally observed nonzero Ti solubility. Apparently, in this case, the E_s is underestimated since it is calculated relative to the LiTiO_2 ($I4_1/amd$) phase, which upon interaction with LiCoO_2 may further decompose into Li_2TiO_3 and Co_3O_4 , with the latter observed experimentally in $\text{LiTi}_x\text{Co}_{1-x}\text{O}_2$ alloys with $x > 0.1$ [61].

Finally, the tetravalent V has positive E_s (0.4 eV), which is in line with the absence of V solubility in LCO. Since the LiVO_2 ($R\bar{3}m$) may further decompose upon interaction with LiCoO_2 , the actual value of E_s may be even larger. Some of the alternative reactions for the calculation of solution energies are compiled in Table S3 in the Supplemental Material [32].

B. Atomic, electronic, and magnetic structure of the (104) surface

To study segregation, we choose the electrochemically active (104) surface (Fig. 2). It has the lowest formation energy in the layered LiCoO_2 for a wide range of oxygen and lithium chemical potentials [9,70,71]. Moreover, the (104) surface is highly important for battery operation, as it exposes Li^+ diffusion channels enabling the (de)intercalation reaction. The (104) surface is nonpolar and fully stoichiometric. Its structure represents an unambiguous termination of the LCO structure along the (104) plane without any reconstruction. As previously shown, Li-Co antisite pairs are thermodynamically unfavorable at the (104) surface [9].

The (104) termination results in undercoordinated Li and Co cations in the topmost layer (Fig. 2). The crystal-field splitting changes for surface Co, as shown in Fig. 3, where octahedral splitting in the bulk region and square pyramidal splitting at the surface are compared. Due to the lowering

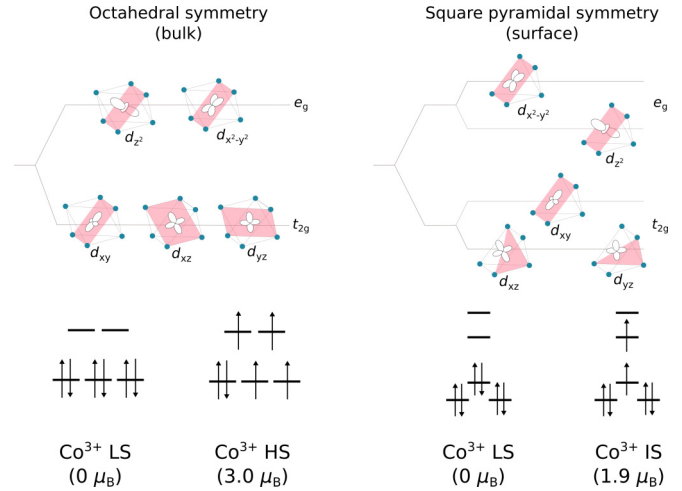


FIG. 3. Crystal field splitting of TM d orbitals for octahedral and square pyramidal coordination. The d -orbital filling for Co^{3+} ions in the bulk [LS and high-spin (HS) states] and at the surface (LS and IS states), with magnetic moments in parentheses.

of d_{xz} , d_{yz} , and d_{z^2} orbitals, the low-spin state of surface Co becomes unstable. Therefore, Co switches to the intermediate spin (IS) state with $1.9 \mu_B$ local magnetic moment [72]. The asymmetry of the spin-up and spin-down states in the case of IS is vividly seen in the local partial density of states (PDOS), compiled in Table S6 in the Supplemental Material [32]. The calculated surface energy of (104) IS is 0.82 J/m^2 . It is 0.3 J/m^2 lower than that of (104) LS. All other obtained spin configurations are compiled in Table S4 in the Supplemental Material [32]. The IS state differs from the LS state by 10% longer Co-O bonds along the c axis (*medial bond*), which can be explained by overlapping Co- d_{z^2} and O- p_z orbitals (Fig. 2 and Fig. S2 in the Supplemental Material [32]).

The calculated surface energy for the IS state is in agreement with the previously published PBE+ U ($U = 3$ eV) value of 0.79 J/m^2 [73]. Another published PBE+ U ($U = 3$ eV) result of 0.3 J/m^2 is significantly underestimated for unknown reasons [74].

C. Surface segregation of dopants at (104)

We investigate the surface segregation trends of LiCoO_2 in its fully lithiated state, as obtained immediately after synthesis. This inquiry is driven by the recognition that the equilibrium segregation of TMs primarily occurs during the high-temperature annealing process of synthesis, rather than through cycling at room temperature, given the inherently low diffusivity of TMs. We provide a brief overview of the influence of lithium concentration on segregation energies in Sec. S6 in the Supplemental Material [32] (see, also, Refs. [75,76] therein).

We study dopant segregation in substitution positions at the topmost surface layer. Due to the formation of APs in the case of Mg, Ti, and V, we consider AP localization both at the surface (S) and the subsurface (U) layers at the INN distance from the dopant (Table S9 in the Supplemental Material [32]). We find that to get the correct electronic states of the Co atoms and dopants, a 224-atom slab with seven atomic

TABLE II. Segregation energies in eV of dopants at the LS/IS (104) LCO surface. The most stable configuration for each dopant with magnetic moments on the dopant and AP is shown (the full lists are collected in Tables S10 and S11 in the Supplemental Material [32]). CoIS is the 1NN Co³⁺ switched from the LS into the IS state.

(104) LCO LS				(104) LCO IS			
Config.	μ_B (M)	μ_B (AP/CoIS)	E_{seg}	Config.	μ_B (M)	μ_B (AP)	E_{seg}
Mg ²⁺ + S AP(Co ⁴⁺)		1.87	-0.75	Mg ²⁺ + U AP(Co ⁴⁺)		1.05	-0.46
Al ³⁺			-0.28	Al ³⁺			-0.04
Ti ⁴⁺ + S AP(Co ²⁺)	0.01	2.67	-1.40	Ti ⁴⁺ + S AP(Co ²⁺)	0.00	2.65	-0.94
V ⁴⁺ + S AP(Co ²⁺)	1.06	2.67	-1.24	V ⁴⁺ + S AP(Co ²⁺)	1.05	2.65	-0.76
Cr ³⁺ HS + S CoIS	2.98	1.92	-0.65	Cr ³⁺ HS	2.99		0.09
Mn ³⁺ LS + S CoIS	3.82	1.90	-1.56	Mn ³⁺ HS	3.83		-0.83
Fe ³⁺ HS + S CoIS	4.19	1.92	-1.08	Fe ³⁺ HS	4.18		-0.45
Ni ³⁺ LS + S CoIS	1.22	1.92	-1.09	Ni ³⁺ LS	1.52		-0.33
				Co ²⁺ HS ^a	2.54		-0.74

^aThe procedure of the Co²⁺ segregation energy calculation is described in Sec. S5.3 in the Supplemental Material [32].

layers is required as followed from our convergence tests (see Tables S5, S7, and S8 in the Supplemental Material [32]). To check the impact of the surface Co spin state on segregation energy, both LS and IS configurations of the (104) surface are studied.

The calculated segregation energies for stable (E_{seg}^s) and all other configurations are compiled in Table II and in Tables S10 and S11 (Supplemental Material [32]), respectively. The E_{seg}^s energies are also shown in Fig. 4 as a function of ionic radii ratio δR .

The first finding is that E_{seg}^s is lower for the LS surface by ~ 0.4 eV than for the IS surface for all dopants. One contributing factor is the higher energy of the LS surface and the absence of penalty related to the different spin states of Co, which are substituted in the bulk and at the surface. Another contributing factor in the case of the LS surface is the transition of one surface Co atom, positioned adjacent to the dopant, from a LS to an IS state (Fig. S3 in the Supplemental Material [32]). However, when the dopant resides within the bulk, all surface Co atoms remain in the LS state. Consequently, when computing the energy difference between the

two slabs, our segregation energy (E_{seg}) can be expressed as the sum of two terms: E_{seg} (all surface Co in LS) + ΔE (Co LS \rightarrow IS). This latter term accounts for the decrease in energy resulting from the transition of one surface Co atom from the LS to the IS state, thus contributing to the decrease in our E_{seg} . Though we employed special measures, such as OMC to converge into correct states, it turned out to be impossible to stabilize the 1NN Co in the LS state. This result shows that it is easy to get a wrong segregation energy using the LS configuration. Further on, we focus on the results obtained for the thermodynamically stable IS surface.

The second finding is that most of the considered dopants (except Al and Cr) have negative segregation energies in the range of -0.33 to -0.94 eV, showing that during annealing of the corresponding solid solutions, the surface should be enriched with doping elements (assuming no repulsion between them at high concentrations). Regarding the reasons for such behavior, we draw attention back to Fig. 4, which suggests that the ionic radius of a dopant may be a key factor affecting the segregation energy. Al, Ni, V, and Ti demonstrate a gradual decrease of segregation energy correlating to the increase of their ionic radius, which becomes, however, random for Cr, Fe, Mn, and Mg. Indeed, it was repeatedly reported that the segregation phenomenon can be driven by the elastic energy contribution due to the atomic/ionic size mismatch between solute and host atoms/ions [77]. Larger solutes may prefer undercoordinated surface positions, which allow easier accommodation of expansive deformation in comparison to bulk, and vice versa. To check this hypothesis, we separate the segregation energy into elastic and chemical contributions according to Eq. (6) and Eq. (7) [56] and plot them in Fig. 5. Looking at the elastic contribution, all cations that are larger than the host Co possess a negative elastic segregation energy, confirming that the expansive deformation at the surface causes a smaller energy penalty than that inside the bulk. In turn, Al³⁺, which is smaller than Co³⁺, has a highly positive elastic contribution, showing that the compressive deformation at the surface is more costly than in the bulk.

It should be admitted though that the interrelation between $E_{\text{seg}}^{\text{elastic}}$ and δR is far from linear. First, it stands out that Al³⁺ is only smaller by 2% than Co³⁺ LS which causes such a huge positive elastic energy penalty in the surface position,

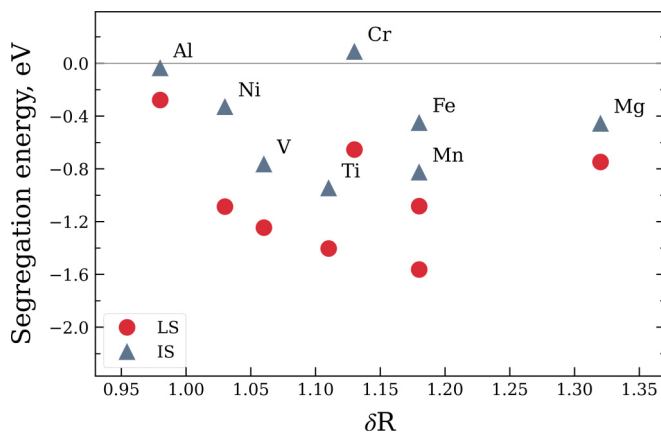


FIG. 4. Segregation energy of considered dopants at the (104) LCO surface with LS and IS states as a function of solute/host ionic radii ratio [Eq. (4)]. In the scenario involving the LS surface, one of the surface Co atoms neighboring the dopant undergoes a transition from a LS to an IS state.

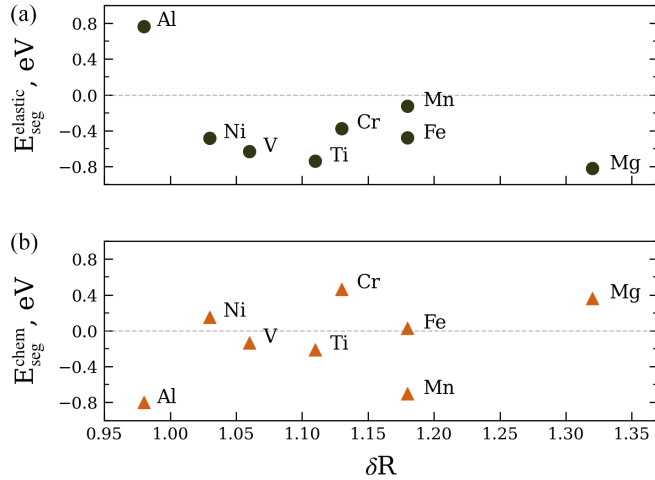


FIG. 5. (a) Elastic and (b) chemical contribution into segregation energy as a function of ionic radii ratio. The calculation procedure is described in Sec. S5 in the Supplemental Material [32].

which is almost fully compensated by a chemical contribution [Fig. 5(b)]. Such behavior is caused by the fact that Al does not have d orbitals which overlap with oxygen p orbitals. As a result, the Al-O interaction is much more ionic compared to the TM-O interactions (the local PDOS confirms the low density of the p -Al states below the Fermi level; see Tables S14 and S15 in the Supplemental Material [32]). At the surface, the Al-O bonds are contracted due to electrostatic attraction, which is especially pronounced for the medial bond (along the c axis), which decreases from 2.05 to 1.85 Å (Table S13 in the Supplemental Material [32]). In other words, the absence of antibonding d states decreases the electrostatic energy of Al^{3+} at the surface, though at the cost of extra elastic energy. By a coincidence, the gain in electrostatic energy and the loss in elastic energy compensate each other almost exactly, which makes Al a nonsegregating element at the (104) surface. This example shows that $E_{\text{seg}}^{\text{elastic}}$ is affected not only by the ionic size mismatch, but also by the chemical nature of the solute. In particular, the absence of d orbitals leads to anisotropic distortion of M-O bonds at the surface.

The next smallest cation is Ni^{3+} LS, which is 3% larger than Co^{3+} LS. Its $E_{\text{seg}}^{\text{elastic}}$ is negative, while $E_{\text{seg}}^{\text{chem}}$ is positive, showing that the driving force for segregation can also be associated with the lattice deformation. Indeed, the extra electron on the e_g orbital causes a Jahn-Teller (JT) distortion of Ni^{3+} both in bulk and at the surface. But since the Co^{3+} is in the LS state (non JT) in bulk and in the IS state (JT) at the surface (Fig. 3), the elastic energy penalty for Ni at the surface is smaller than in the bulk. In other words, the surface position of Co is already JT distorted and requires minimal deformations upon substitution with Ni. The opposite is true when Ni substitutes for Co in the bulk position, causing more deformations of the surrounding lattice due to the introduction of JT distortions. This example demonstrates again that the $E_{\text{seg}}^{\text{elastic}}$ contribution is affected not only by the ionic size mismatch, but also by the chemical nature of the solute element, in this case its ability to produce JT distortion.

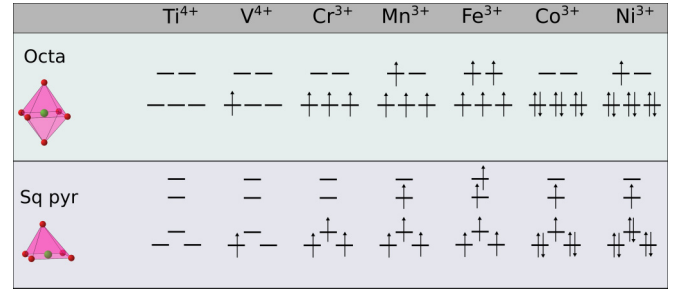


FIG. 6. Crystal field splitting of TM d orbitals for octahedral and square pyramidal coordination.

The next two solutes followed in the order of increasing ionic radii are V^{4+} and Ti^{4+} . The peculiarity of these solutes is that they represent M-AP complexes, which makes their analysis tricky. Our calculations show that the segregation of a small hole polaron is itself favorable with E_{seg} of -0.7 eV, which is an important contribution for Ti and V segregation. In the case of V^{4+} , a shortening of one vanadyl-like bond (1.8 Å) manifests only at the surface, where less-constraining conditions are realized. Apparently, this effect slightly lowers V segregation energy. Anyway, the negative $E_{\text{seg}}^{\text{elastic}}$, which decreases with the ionic radius, serves as a considerable driving force for segregation. Here, accommodation of expansive deformations around the solute and Co^{2+} small polaron is easier at the surface than in the bulk.

Cr^{3+} destroys the trend of $E_{\text{seg}}^{\text{elastic}}$ decrease despite its even larger radius, though $E_{\text{seg}}^{\text{elastic}}$ remains negative. Moreover, Cr^{3+} demonstrates a quite positive $E_{\text{seg}}^{\text{chem}}$ contribution which fully compensates the elastic contribution making Cr a nonsegregating dopant. The small elastic gain may be related to the fact that Cr^{3+} is lacking the e_g electron responsible for JT distortion of a surface site (see Fig. 6).

The next two solutes, Mn^{3+} and Fe^{3+} , have the same ionic radii, but demonstrate a somewhat different behavior. Mn has zero $E_{\text{seg}}^{\text{elastic}}$, while Fe has -0.5 eV. It is hard to rationalize such behavior, but from the M-O distances, it is seen that Mn has a much longer medial M-O bond of 2.13 Å, which may be a reason for the additional energy penalty. Overall, both Fe and Mn strongly distort both bulk and surface sites with the distinction that Mn^{3+} is JT active and Fe^{3+} is not (Fig. 6).

The last and largest considered solute is Mg^{2+} , which reveals the most negative $E_{\text{seg}}^{\text{elastic}}$, confirming the initial hypothesis that expansive relaxation is easier at the surface than in the bulk. However, the situation is complicated by the formation of an additional small polaron hole, which is located at the subsurface layer and may have an additional impact on the $E_{\text{seg}}^{\text{elastic}}$ value.

Recently, Dahl *et al.* [23] reported a linear dependence of segregation energy on the solute's ionic radius, calculated using empirical Coulomb-Buckingham potentials for the (104) surface of LCO. However, the linear dependence is maintained only within solutes with the same valency having no partially filled d orbitals, in particular for Sc^{3+} , Y^{3+} , Gd^{3+} , La^{3+} , for Mg^{2+} , Ca^{2+} , Sr^{2+} , and for Ti^{4+} , Sn^{4+} , Zr^{4+} .

We show that when cations do contain d orbitals (Ni^{3+} , Cr^{3+} , Fe^{3+} , Mn^{3+}), no linear dependence of segregation

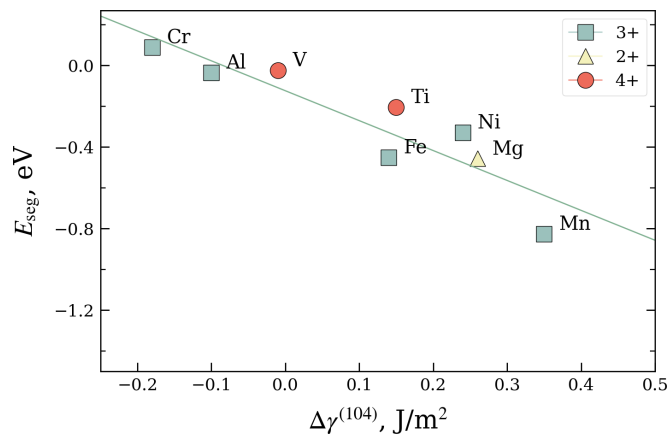


FIG. 7. Segregation energy of dopants as a function of $\Delta\gamma^{(104)}$ [$\Delta\gamma^{(104)} = \gamma^{(104)}(\text{LiCoO}_2) - \gamma^{(104)}(\text{LiMO}_2)$]. For Ti and V, the segregation energy of the small polaron electron (-0.74 eV) is subtracted. The Pearson correlation coefficient is -0.872 . Magnetic structures of LiMO_2 are collected in Table S17 in the Supplemental Material [32].

energy on the ionic radius is observed. Also, the divalent and trivalent elements produce additional polarons that have an important impact on E_{seg} . We admit that the ionic radius may help to predict the sign of the segregation energy, but apart from that, the ionic size mismatch arguments give little explanation of the observed behavior of segregation energies; rather, the full geometry of the surface and bulk sites should be analyzed.

To improve the understanding of the obtained trends, we recall other descriptors of E_{seg} , in particular the findings of Alden *et al.* [78–80] and Ruban *et al.* [81,82], who showed that for simple, rare-earth, and transition metals, the main contribution to the surface segregation energy is given by the difference in the surface energies between the solute and the host. To check whether this is true for layered oxides we calculated these differences ($\Delta\gamma$) using the (104) surface of the LiMO_2 ($R\bar{3}m$) phase for all solutes, which is shown in Fig. 7 (energies and magnetic structures are collected in Table S17 in the Supplemental Material [32] and [83]).

To our satisfaction, E_{seg} shows excellent correlation with $\Delta\gamma$ across +2, +3, and +4 elements after correction for additional polarons. The obtained result gives a very clear physical picture. Those solutes that have smaller LiMO_2 surface energies than LiCoO_2 are more prone to segregation. The elastic gain explains why segregation energies of larger cations are additionally shifted down, e.g., making E_{seg} for Cr equal to zero, despite the larger surface energy of LiCrO_2 than that of LiCoO_2 . Al is a special case: despite its higher surface energy, its segregation energy is lowered by the electrostatic energy gain at a surface site due to the absence of repulsion from d orbitals.

The discovered relationship between differential surface energy and segregation energy seems natural; however, it is far from obvious. The existence of such relationship indicates that most of the electronic effects are confined within the MO_6/MO_5 polyhedra. The local electronic structure of one solute atom M inside LCO is, in fact, very similar to that inside of bulk LiMO_2 . Such locality reveals that the

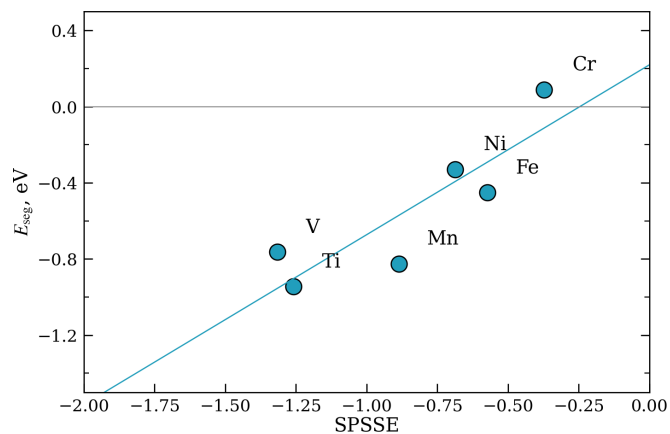


FIG. 8. Segregation energy as a function of the square pyramidal-site stabilization energy (SPSSE) of d metals. The Pearson correlation coefficient is 0.860.

surface segregation trend can be captured by a simple local descriptor related to a polyhedron. One possible choice is the *stabilization energy* defined within the crystal-field theory [84]. Using this theory, we calculate stabilization energies for octahedral and square pyramidal polyhedra for Co and dopant and derive a differential square pyramidal-site stabilization energy (SPSSE), showing the preference of a square pyramidal site at the surface over an octahedral site in the bulk. The details of the calculation are provided in Sec. S5.5 in the Supplemental Material [32], while E_{seg} as a function of SPSSE is shown in Fig. 8. It is seen that E_{seg} has excellent correlation with SPSSE, confirming the above hypothesis that the main contribution to segregation energy is governed by the local d -orbital splitting, while the band structure effects are of less importance. The SPSSE value may serve as an effective descriptor of TM segregation energies in other layered oxides.

IV. DISCUSSION

A. On the comparison of calculated solution energies and experimentally observed solubilities

Discussing the solubility of the considered elements, we divide them into three groups. The first group is represented by Ni, Al, and Cr, which allows one to easily synthesize the LiMO_2 ($R\bar{3}m$) layered phase isostructural to LCO [85,86]. According to our calculations, all of them have slightly positive solution energies, showing that at low concentrations, the solubility is driven by entropy factors, while at higher concentration, there should be an additional stabilization of solid solutions due to M-M interactions. Ni is the main alloying element for Co-based oxides, and a single-phase layered $\text{LiCo}_{1-x}\text{Ni}_x\text{O}_2$ can be synthesized in the whole range of x [66,67,87]. The $\text{LiCo}_{1-x}\text{Al}_x\text{O}_2$ solid solution can be successfully synthesized with $x \leq 0.6$ – 0.8 , depending on the synthesis procedure [26,59,60]. Ceder *et al.* reported the smallest formation enthalpy of $\text{Li}(\text{Co}, \text{Al})\text{O}_2$ among 3+ elements leading to the entropy-driven mixing between Co and Al [68]. $\text{LiCo}_{1-x}\text{Cr}_x\text{O}_2$ also can be successfully synthesized as a layered single-phase compound for $x = 0$ – 0.5 [27,88].

The second group of dopants is represented by Mn and Fe, which can exist as a layered oxide, but due to its thermodynamic instability, their synthesis is possible only via Na/Li cation exchange. According to our findings, Mn has a moderately positive solution energy, which is consistent with the theoretical investigation of Koyama *et al.*, who showed that layered $\text{LiCo}_{1-x}\text{Mn}_x\text{O}_2$ cannot be prepared as a stable phase in the entire range of x [89]. Although, several studies claim the possibility of a $R\bar{3}m$ solid solution with the Mn concentration up to 0.2 [63,64,90], Mn addition increases structural disorder, leading to the transformation from a layered trigonal to the rock-salt cubic structure [63]. Julien *et al.* also showed the formation of a modified-spinel structure ($Fd\bar{3}m$) for the $\text{LiCo}_{0.5}\text{Mn}_{0.5}\text{O}_2$ composition [58]. It is known that the solid solutions between LCO- Li_2MnO_3 on the whole range of Mn content are more probable [69,91]. A single-phase iron-doped $\text{LiCo}_{1-x}\text{Fe}_x\text{O}_2$ with ($R\bar{3}m$) symmetry can be obtained via hydrothermal reaction for compositions with $x \leq 0.25$ [28,65]. At a higher Fe content, a second-phase $\alpha\text{-LiFeO}_2$ with a cubic rock-salt structure is forming [28].

The third group of dopants is represented by divalent/tetravalent dopants (Mg, Ti, and V), which lead to the presence of $\text{Co}^{4+}/\text{Co}^{2+}$ charge compensators [61,92]. Although the majority of works are devoted to the Mg-doped LCO with a Mg content less than 5–10% [93], which was obtained as a Mg solution limit [92], Julien *et al.* reported the possibility of synthesizing a single-phase $\text{LiMg}_{0.5}\text{Co}_{0.5}\text{O}_2$ with a small amount of some secondary phase. Moreover, at low concentration, Mg (1%) fills Li vacancies, but upon increasing concentration, it substitutes Co, creating an equal number of Co^{4+} for charge balance [92,94]. A similar situation is observed in LiNiO_2 (LNO), where Mg occupies Ni positions at concentrations higher than 10% [95]. Our calculations predict $\text{Co}_{\text{Li}} + \text{AP}$ (Co^{4+}) substitution as most stable ($E_s = 0.08$ eV), followed by 0.5 eV higher $\text{Mg}_{\text{Li}}\text{-Mg}_{\text{Co}}$ complex, and by 0.8 eV higher $\text{Mg}_{\text{Li}} + \text{AP}$ (Co^{2+}) substitution (Table S2 in the Supplemental Material [32]). Overall, the slightly positive solution energies in the first case are in line with relatively good Mg solubility.

It is known that the layered Ti-based oxide cannot be easily synthesized due to cation disordering at the synthesis temperature [85,96]. Several studies report low solubility of Ti in LCO (<5–10%), noting that Ti addition corresponds to Co substitution in the CoO_2 layers, with Co^{2+} being the charge compensator [16,61,97]. Low solubility of Ti contradicts with our calculated solution energy, which is moderately negative. However, we calculated Ti solution energy with respect to the lowest-energy polymorph of LiTiO_2 ($I4_1/amd$), although numerous experimental works report Li_2TiO_3 as a secondary phase. The solution energy of Ti relative to the $0.5[\text{Li}_2\text{TiO}_3 + \text{TiO}_2 - 0.5\text{O}_2(\text{gas}, 1000 \text{ K})]$ is ~ 1 eV (Table S3 in the Supplemental Material [32]), which may explain poor Ti solubility.

Although the lowest-energy LiVO_2 phase is isostructural to LCO, the solution energy of V^{4+} is moderately positive in LCO, explaining the absence of experimental reports of V-containing LCO solid solutions. This is consistent with the computational study (PBE+ U) of Ma *et al.* [98], who obtained very high formation energy of layered $\text{LiCo}_{0.5}\text{V}_{0.5}\text{O}_2$ and claimed the impossibility of solid solution existence. The preference of V^{4+} over V^{5+} in our calculations is supported

by the experimental results of Han *et al.*, who reported the 4+ oxidation state of vanadium in Li-rich NMC [99].

B. Comparison of segregation behavior with experimental observations

The comparison of computational results on segregation with experiment is troublesome. In computational studies, the segregation is confined to a couple of outermost atomic layers, which aligns with a strict definition of *surface segregation*. Contrary to that, in experimental studies, a much thicker dopant-enriched surface layer (1–10 nm) may be voluntarily classified as a *surface segregation* phenomenon. In our opinion, such a surface layer better fits under the definition of a *surface phase*. However, its formation should be preceded by a nucleation, e.g., by means of surface segregation in its strict meaning. Therefore, in further discussion, we will compare our results for segregation in the outermost single layer with multilayered dopant-enriched surface regions.

Our calculations show that surface segregation is favorable for $\text{Mg}_{\text{Co}} - \text{AP}$ (−0.5 eV), $\text{Mg}_{\text{Li}} - \text{AP}$ (−0.5 eV), and $\text{Mg}_{\text{Li}} - \text{Mg}_{\text{Co}}$ complexes (−0.6 eV). No experimental reports for only Mg-doped LCO observe enhanced Mg concentration at the surface. A possible explanation may be rooted in the fact that Mg migration is highly prohibited, requiring high-temperature annealing to obtain equilibrium segregation. There exists an energy-dispersive x-ray spectroscopy (EDS) mapping of a Mg-enriched surface region in a Mg-Al-Eu co-doped LCO [25]; however, this region can hardly be classified even as a surface phase. Since the refractory MgO (melting $T = 2852$ °C) was used as a precursor in the synthesis, the enriched region may appear due to incomplete homogenization of Mg.

In the case of Al, the calculated segregation energy is only −0.04 eV, which is comparable with kT energy at room temperature, making Al a nonsegregating element. Indeed, according to the XPS study of only Al-doped $\text{LiCo}_{1-x}\text{Al}_x\text{O}_2$ solid solutions ($x = 0.15, 0.25, 0.5$), no Al surface segregation was detected [26]. The same should be true for Cr, which has nearly zero segregation energy. An experimental study confirming this finding would be of fundamental interest.

Ti, according to our calculations, should be a strongly segregating element ($E_{\text{seg}} = -0.94$ eV), which aligns with multiple experimental observations of Ti enrichment at the LCO surface. Zhang *et al.*, using EDS mapping and EELS methods, observed surface Ti enrichment in $\text{LiTi}_{0.001}\text{Mg}_{0.001}\text{Al}_{0.001}\text{Co}_{0.997}\text{O}_2$ [15], which spans up to 10 nm at the edge of the particle. Their DFT PBE+ U ($U = 4.91$ and 5.0 eV for Co and Ti) calculations gave −0.7 eV segregation energy, in good agreement with our result. Hong *et al.* confirmed Ti surface enrichment in only Ti-doped (0.1%wt) LCO using elemental depth profiling within hard x-ray nanofluorescence mapping [16]. Finally, Li *et al.* [20] clearly demonstrated that Ti surface enrichment discovered with EDS mapping has a thermodynamic origin, since the increase of surface Ti concentration takes place upon high-temperature annealing of a $\text{LiTi}_{0.005}\text{Co}_{0.995}\text{O}_2$ solid solution. They show that Ti prefers only the non-(003) surfaces, e.g., (104), and improves electrochemical cycling.

The atomic resolution high-angle annular dark-field scanning transmission electron microscopy (HAADF-STEM) image suggests that the observed Ti concentration enhancement is confined within the 1 nm outermost region, which can be classified as *surface segregation* in its strict sense. In the case of V, the segregation is also favorable (−0.76 eV); therefore, despite the absent solubility in LCO, V may still serve as a surface dopant. No experimental studies are yet available to check this hypothesis. Despite considerable solubility of Fe [100], the experimental studies of Fe-doped LCO are scarce. The surface concentration was never investigated investigated. At the same time, the relatively strong tendency for segregation (−0.45 eV) obtained in our calculations justifies such studies. The remaining two elements Mn and Ni are practically important. We found Mn³⁺ to be a strongly segregating element with $E_{\text{seg}} = -0.83$ eV. On first sight, this is in contradiction to the EDS mapping of Ni-Mn co-doped LiNi_{0.05}Co_{0.9}Mn_{0.05}O₂ performed by Wang *et al.*, who observed no Mn or Ni segregation [101]. However, the reason for this is that in a co-doped sample, Mn and Ni have +4 and +2 oxidation states, respectively. In turn, our calculation predicts that in single-doped samples, both Mn and Ni should be in the +3 state (Table S2 in the Supplemental Material [32]). Indeed, the experimental studies of LiCo_{1-x}Mn_xO₂ solid solutions suggest that Mn is in the +3 oxidation state [64,102]. Interestingly, besides the important role of Mn, we find no experimental data on Mn segregation in only Mn-doped LCO. At the same time, 5% Mn doping improves the high-voltage electrochemical behavior of LiCoO₂ [103], which justifies a more careful examination of Mn surface segregation in single-doped LCO. Finally, our calculations predict that segregation of Ni³⁺ is moderately favorable with E_{seg} of −0.33 eV. This result aligns with Yoon *et al.*, who observed an enhancement of surface Ni concentration using spatially resolved EELS for a single-doped LiCo_{0.95}Ni_{0.05}O₂ [24]. The enhancement extends up to 40 nm and resembles a Ni-enriched surface phase. Therefore, it is still to be shown whether its formation is triggered by a monolayer surface segregation. Anyway, the Ni enhancement promotes beneficial reconstruction with the formation of a stable cation-mixed phase that slows down oxygen loss.

We should mention that surface segregation does not guarantee an improved stability of a particle surface. On the contrary, the decrease of surface energy upon surface segregation may be accompanied with the weakening of M-O bonds, promoting oxygen release and surface structure reconstruction. Experimental studies have widely established that LiNiO₂ or Ni-rich layered oxides exhibit a higher tendency for oxygen release compared to LiCoO₂ [104,105]. This observation is further supported by DFT calculations of surface oxygen vacancies' formation energies (E_{vac}), commonly utilized as a descriptor of oxygen stability [106,107]. For instance, E_{vac} in LiNiO₂ is calculated at 1.1 eV, while in LiCoO₂, it stands at 1.8 eV in the fully intercalated state, with a significant decrease upon deintercalation [108]. Consequently, the segregation of nickel is expected to facilitate oxygen release, potentially elucidating the observed negative impact of nickel segregation reported in previous studies [18,19].

The trends observed in E_{vac} across different transition metals and levels of intercalation are not straightforward. During deintercalation, E_{vac} in LiCoO₂ decreases from 1.8 to 0.4 eV, whereas in LiMnO₂, it decreases from 3.2 to 0.8 eV [108]. This indicates that manganese segregation can enhance oxygen stability, particularly in deintercalated states. However, this analysis is valid only if the surface maintains its layered structure and remains unreconstructed. Upon reconstruction into spinel or rock-salt structures, the role of dopants may vary, as demonstrated by Yoon, where Ni-induced reconstruction proved beneficial [24]. Such surface transformations to reduced spinel-like and rock-salt structures are well documented [104]. While they are often viewed as detrimental, they also serve a protective function by mitigating further oxygen release. The issue arises when the layer becomes too thick, hindering lithium diffusion. In this manner, surface segregation may serve as a catalyst for electrochemically more favorable reconstructions.

Another indirect consequence of surface segregation may lie in its influence on the migration barriers of oxygen vacancies. Studies have shown that oxygen vacancies formed at the surface have a propensity to diffuse inward, contributing to material degradation [104]. It is conceivable that certain segregating elements, while facilitating the formation of vacancies, may also immobilize them by promoting stronger M-v_O bonding and increasing the migration barrier for oxygen vacancies. This impediment could restrict their diffusion either inward towards the bulk or across the surface, preventing the formation of oxygen vacancy clusters. The clustering of oxygen vacancies is known to be highly detrimental [104]; therefore, the impact of segregation on clustering should also be thoroughly investigated.

In addition to oxygen vacancies, the formation of surface Li-TM antisites represents another crucial process, particularly during the transformation from layered to spinel and rock-salt structures. Previous research employing DFT+*U* calculations has demonstrated that the formation of Li-TM antisite pairs is more favorable at the surface compared to the bulk [9], thus providing insight into the surface's inclination towards reconstruction. However, the influence of segregation on surface antisites remains an open question and warrants further investigation.

Therefore, the effects of surface segregation and the formation of surface phases should be carefully evaluated in terms of their beneficial and detrimental impact on electrochemical performance of a battery. In summary, our calculations for LCO correlate with experimental observation of Ti, and Ni surface enhancement, as well as the absence of Al segregation. We predict strong segregation of Mn³⁺ and V⁴⁺, moderate segregation of Fe³⁺ and Mg²⁺, and no segregation of Cr³⁺ dopants, justifying further experimental investigation of LCO surface compositions.

V. CONCLUSIONS

Using DFT-PBE+*U*, we investigated the bulk solution and surface segregation of Mg, Al, Ti, V, Cr, Mn, Fe, and Ni elements at the (104) surface of LiCoO₂ ($R\bar{3}m$), leading to the following conclusions:

(i) All elements except for V have either negative or slightly positive solution energies for the M_{Co} position, which is in agreement with the experimentally observed solubilities.

(ii) For trivalent elements, the solution energy increases with the ionic radius. Divalent (Mg) and tetravalent (Ti and V) substitutions invoke the formation of an additional small polaron hole and small polaron electron at the 1NN Co site, respectively.

(iii) The energy of the (104) surface is 0.82 J/m^2 . The Co at the surface has a pyramidal coordination, which stabilizes the intermediate spin (IS) configuration with a local magnetic moment of $2 \mu_B$. The employment of slabs with an IS state of surface Co is vitally important to obtain correct segregation energies.

(iv) All elements, except for Cr and Al, have negative segregation energies ranging from -0.3 eV for Ni to -0.9 eV for Ti, showing that the (104) surface of LiCoO_2 should be enriched with these solutes.

(v) The segregation energy of solute M linearly correlates with the energy of the (104) surface of the LiMO_2 ($R\bar{3}m$) phase, revealing that the main driving force for segregation is connected with the M-O bond-breaking penalty.

(vi) The main contribution to segregation energy has a local nature and can be described within crystal-field theory using differential stabilization energy.

(vii) The secondary driving force for segregation is related with the elastic energy penalty due to the ionic size effect. Larger cations gets additional gain at the surface. The segregation of Ti and V is additionally stabilized by small polaron holes, which prefer to be at the surface.

(viii) The strongly segregating elements such as Fe, Ni, Mg, and Mn should play an important role as alloying elements due to their increased concentration at the electrochemically active (104) surface, which requires additional experimental investigation.

ACKNOWLEDGMENT

A.O.B., A.M.A., and D.A.A. acknowledge the financial support of the Russian Science Foundation Project No. 23-73-30003.

-
- [1] A. Manthiram, *Nat. Commun.* **11**, 1550 (2020).
- [2] A. Savina, A. Boev, E. Orlova, A. Morozov, and A. Abakumov, *Russian Chem. Rev.* **92**, RCR5086 (2023).
- [3] A. M. Abakumov, S. S. Fedotov, E. V. Antipov, and J.-M. Tarascon, *Nat. Commun.* **11**, 4976 (2020).
- [4] J. B. Goodenough and Y. Kim, *Chem. Mater.* **22**, 587 (2010).
- [5] F. Lin, I. M. Markus, D. Nordlund, T.-C. Weng, M. D. Asta, H. L. Xin, and M. M. Doeff, *Nat. Commun.* **5**, 3529 (2014).
- [6] C. Tian, F. Lin, and M. M. Doeff, *Acc. Chem. Res.* **51**, 89 (2018).
- [7] D. Aksyonov, A. Boev, S. Fedotov, and A. Abakumov, *Solid State Ion.* **393**, 116170 (2023).
- [8] C. Liang, R. C. Longo, F. Kong, C. Zhang, Y. Nie, Y. Zheng, and K. Cho, *ACS Appl. Mater. Interfaces* **10**, 6673 (2018).
- [9] A. Boev, S. Fedotov, A. Abakumov, K. Stevenson, G. Henkelman, and D. Aksyonov, *Appl. Surf. Sci.* **537**, 147750 (2021).
- [10] H. Zhang, B. M. May, J. Serrano-Sevillano, M. Casas-Cabanas, J. Cabana, C. Wang, and G. Zhou, *Chem. Mater.* **30**, 692 (2018).
- [11] M. Bianchini, M. Roca-Ayats, P. Hartmann, T. Brezesinski, and J. Janek, *Angew. Chem., Intl. Ed.* **58**, 10434 (2019).
- [12] C. Xu, K. Märker, J. Lee, A. Mahadevegowda, P. J. Reeves, S. J. Day, M. F. Groh, S. P. Emge, C. Ducati, B. Layla Mehdi *et al.*, *Nat. Mater.* **20**, 84 (2021).
- [13] R. Lin, E. Hu, M. Liu, Y. Wang, H. Cheng, J. Wu, J.-C. Zheng, Q. Wu, S. Bak, X. Tong *et al.*, *Nat. Commun.* **10**, 1650 (2019).
- [14] J. Cheng, L. Mu, C. Wang, Z. Yang, H. L. Xin, F. Lin, and K. A. Persson, *J. Mater. Chem. A* **8**, 23293 (2020).
- [15] J.-N. Zhang, Q. Li, C. Ouyang, X. Yu, M. Ge, X. Huang, E. Hu, C. Ma, S. Li, R. Xiao *et al.*, *Nat. Energy* **4**, 594 (2019).
- [16] Y.-S. Hong, X. Huang, C. Wei, J. Wang, J.-N. Zhang, H. Yan, Y. S. Chu, P. Pianetta, R. Xiao, X. Yu *et al.*, *Chem* **6**, 2759 (2020).
- [17] S. Guo, Q. Li, P. Liu, M. Chen, and H. Zhou, *Nat. Commun.* **8**, 135 (2017).
- [18] H. Dixit, W. Zhou, J.-C. Idrobo, J. Nanda, and V. R. Cooper, *ACS Nano* **8**, 12710 (2014).
- [19] P. Yan, J. Zheng, J. Zheng, Z. Wang, G. Teng, S. Kuppan, J. Xiao, G. Chen, F. Pan, J.-G. Zhang *et al.*, *Adv. Energy Mater.* **6**, 1502455 (2016).
- [20] J. Li, Z. Zhang, C. Qin, Y. Jiang, X. Han, Y. Xia, M. Sui, and P. Yan, *Small* **19**, 2303474 (2023).
- [21] Y. Wang, Q. Zhang, Z.-C. Xue, L. Yang, J. Wang, F. Meng, Q. Li, H. Pan, J.-N. Zhang, Z. Jiang *et al.*, *Adv. Energy Mater.* **10**, 2001413 (2020).
- [22] Y. Shin, W. H. Kan, M. Aykol, J. K. Papp, B. D. McCloskey, G. Chen, and K. A. Persson, *Nat. Commun.* **9**, 4597 (2018).
- [23] S. Dahl, T. Aoki, A. Banerjee, B. P. Uberuaga, and R. H. Castro, *Chem. Mater.* **34**, 7788 (2022).
- [24] M. Yoon, Y. Dong, Y. Yoo, S. Myeong, J. Hwang, J. Kim, S.-H. Choi, J. Sung, S. J. Kang, J. Li *et al.*, *Adv. Funct. Mater.* **30**, 1907903 (2020).
- [25] X. Tan, Y. Zhang, S. Xu, P. Yang, T. Liu, D. Mao, J. Qiu, Z. Chen, Z. Lu, F. Pan *et al.*, *Adv. Energy Mater.* **13**, 2300147 (2023).
- [26] L. Dahéron, R. Dedryvère, H. Martinez, D. Flahaut, M. Ménétrier, C. Delmas, and D. Gonbeau, *Chem. Mater.* **21**, 5607 (2009).
- [27] C. Jones, E. Rossen, and J. Dahn, *Solid State Ion.* **68**, 65 (1994).
- [28] M. Tabuchi, K. Ado, H. Kobayashi, H. Sakaebe, H. Kageyama, C. Masquelier, M. Yonemura, A. Hirano, and R. Kanno, *J. Mater. Chem.* **9**, 199 (1999).
- [29] J. P. Perdew, K. Burke, and M. Ernzerhof, *Phys. Rev. Lett.* **77**, 3865 (1996).
- [30] G. Kresse and J. Furthmüller, *Phys. Rev. B* **54**, 11169 (1996).

- [31] S. L. Dudarev, G. A. Botton, S. Y. Savrasov, C. J. Humphreys, and A. P. Sutton, *Phys. Rev. B* **57**, 1505 (1998).
- [32] See Supplemental Material at <http://link.aps.org/supplemental/10.1103/PhysRevMaterials.8.055403> for a detailed characterization of the electronic and atomic structure of configurations with dopants, an extended description of the methodology used, and additional benchmarking information.
- [33] A. Jain, G. Hautier, C. J. Moore, S. P. Ong, C. C. Fischer, T. Mueller, K. A. Persson, and G. Ceder, *Comput. Mater. Sci.* **50**, 2295 (2011).
- [34] O. Y. Long, G. S. Gautam, and E. A. Carter, *Phys. Chem. Chem. Phys.* **23**, 24726 (2021).
- [35] W. Tian, M. Chisholm, P. Khalifah, R. Jin, B. Sales, S. Nagler, and D. Mandrus, *Mater. Res. Bull.* **39**, 1319 (2004).
- [36] H. Elsaedy, *J. Electron. Mater.* **49**, 282 (2020).
- [37] A. Chakraborty, M. Dixit, D. Aurbach, and D. T. Major, *npj Comput. Mater.* **4**, 60 (2018).
- [38] F. Kong, R. C. Longo, M.-S. Park, J. Yoon, D.-H. Yeon, J.-H. Park, W.-H. Wang, K. Santosh, S.-G. Doo, and K. Cho, *J. Mater. Chem. A* **3**, 8489 (2015).
- [39] V. R. Galakhov, E. Z. Kurmaev, St. Uhlenbrock, M. Neumann, D. G. Kellerman, and V. S. Gorshkov, *Solid State Commun.* **95**, 347 (1995).
- [40] K. Kushida and K. Kuriyama, *Solid State Commun.* **123**, 349 (2002).
- [41] J. van Elp, J. Wieland, H. Eskes, P. Kuiper, G. Sawatzky, F. De Groot, and T. Turner, *Phys. Rev. B* **44**, 6090 (1991).
- [42] S. Laubach, S. Laubach, P. C. Schmidt, D. Enslin, S. Schmid, W. Jaegermann, A. Thißen, K. Nikolowski, and H. Ehrenberg, *Phys. Chem. Chem. Phys.* **11**, 3278 (2009).
- [43] D.-H. Seo, A. Urban, and G. Ceder, *Phys. Rev. B* **92**, 115118 (2015).
- [44] W. Sun and G. Ceder, *Surf. Sci.* **617**, 53 (2013).
- [45] J. P. Allen and G. W. Watson, *Phys. Chem. Chem. Phys.* **16**, 21016 (2014).
- [46] S. Grimme, J. Antony, S. Ehrlich, and H. Krieg, *J. Chem. Phys.* **132**, 154104 (2010).
- [47] S. Grimme, S. Ehrlich, and L. Goerigk, *J. Comput. Chem.* **32**, 1456 (2011).
- [48] J. M. Rosolen and F. Decker, *J. Electroanal. Chem.* **501**, 253 (2001).
- [49] M. Rao and O. Hussain, *Eur. Phys. J. Appl. Phys.* **48**, 20503 (2009).
- [50] K. Kushida and K. Kuriyama, *Solid State Commun.* **118**, 615 (2001).
- [51] A. Jain, S. P. Ong, G. Hautier, W. Chen, W. D. Richards, S. Dacek, S. Cholia, D. Gunter, D. Skinner, G. Ceder *et al.*, *APL Mater.* **1**, 011002 (2013).
- [52] D. Aksyonov, S. Fedotov, K. Stevenson, and A. Zhugayevych, *Comput. Mater. Sci.* **154**, 449 (2018).
- [53] A. Jain, G. Hautier, S. P. Ong, C. J. Moore, C. C. Fischer, K. A. Persson, and G. Ceder, *Phys. Rev. B* **84**, 045115 (2011).
- [54] R. D. Shannon, *Acta Crystallogr., Sect. A: Cryst. Phys., Diffraction, Theor. Gen. Crystallogr.* **32**, 751 (1976).
- [55] D. Aksyonov, A. Lipnitskii, and Y. R. Kolobov, *Modell. Simul. Mater. Sci. Eng.* **21**, 075009 (2013).
- [56] D. A. Aksyonov, T. Hickel, J. Neugebauer, and A. Lipnitskii, *J. Phys.: Condens. Matter* **28**, 385001 (2016).
- [57] H.-S. Kim, T.-K. Ko, B.-K. Na, W. I. Cho, and B. W. Chao, *J. Power Sources* **138**, 232 (2004).
- [58] C. Julien, M. Camacho-Lopez, T. Mohan, S. Chitra, P. Kalyani, and S. Gopukumar, *Solid State Ion.* **135**, 241 (2000).
- [59] E. Gaudin, F. Taulelle, R. Stoyanova, E. Zhecheva, R. Alcantara, P. Lavela, and J. Tirado, *J. Phys. Chem. B* **105**, 8081 (2001).
- [60] Y. Takahashi, N. Kijima, and J. Akimoto, *J. Solid State Chem.* **178**, 3667 (2005).
- [61] S. Gopukumar, Y. Jeong, and K. B. Kim, *Solid State Ion.* **159**, 223 (2003).
- [62] W. Huang and R. Frech, *Solid State Ion.* **86-88**, 395 (1996).
- [63] R. Stoyanova, E. Zhecheva, and L. Zarkova, *Solid State Ion.* **73**, 233 (1994).
- [64] P. Suresh, S. Rodrigues, A. Shukla, H. Vasan, and N. Munichandraiah, *Solid State Ion.* **176**, 281 (2005).
- [65] R. Alcantara, J. Jumas, P. Lavela, J. Olivier-Fourcade, C. Pérez-Vicente, and J. Tirado, *J. Power Sources* **81-82**, 547 (1999).
- [66] C. Delmas and I. Saadoune, *Solid State Ion.* **53-56**, 370 (1992).
- [67] M. Wang and A. Navrotsky, *Solid State Ion.* **166**, 167 (2004).
- [68] G. Ceder, Y.-M. Chiang, D. Sadoway, M. Aydinol, Y.-I. Jang, and B. Huang, *Nature (London)* **392**, 694 (1998).
- [69] K. Numata, C. Sakaki, and S. Yamanaka, *Solid State Ion.* **117**, 257 (1999).
- [70] D. Kramer and G. Ceder, *Chem. Mater.* **21**, 3799 (2009).
- [71] A. V. Morozov, H. Paik, A. O. Boev, D. A. Aksyonov, S. A. Lipovskikh, K. J. Stevenson, J. L. Rupp, and A. M. Abakumov, *ACS Appl. Mater. Interfaces* **14**, 39907 (2022).
- [72] D. Carlier, J.-H. Cheng, C.-J. Pan, M. Menetrier, C. Delmas, and B.-J. Hwang, *J. Phys. Chem. C* **117**, 26493 (2013).
- [73] L. Hong, L. Hu, J. W. Freeland, J. Cabana, S. Ogut, and R. F. Klie, *J. Phys. Chem. C* **123**, 8851 (2019).
- [74] D. Qian, Y. Hinuma, H. Chen, L.-S. Du, K. J. Carroll, G. Ceder, C. P. Grey, and Y. S. Meng, *J. Am. Chem. Soc.* **134**, 6096 (2012).
- [75] J. Li, R. Doig, J. Camardese, K. Plucknett, and J. R. Dahn, *Chem. Mater.* **27**, 7765 (2015).
- [76] H. Ben Yahia, M. Shikano, and H. Kobayashi, *Chem. Mater.* **25**, 3687 (2013).
- [77] A. Kartamyshev, D. Poletaev, A. Boev, and D. Aksyonov, *Comput. Mater. Sci.* **230**, 112517 (2023).
- [78] M. Aldén, I. A. Abrikosov, B. Johansson, N. M. Rosengard, and H. L. Skriver, *Phys. Rev. B* **50**, 5131 (1994).
- [79] M. Aldén, H. L. Skriver, and B. Johansson, *Phys. Rev. B* **50**, 12118 (1994).
- [80] M. Aldén, B. Johansson, and H. L. Skriver, *Phys. Rev. B* **51**, 5386 (1995).
- [81] A. V. Ruban, H. L. Skriver, and J. K. Nørskov, *Phys. Rev. B* **59**, 15990 (1999).
- [82] A. Ruban and H. L. Skriver, *Comput. Mater. Sci.* **15**, 119 (1999).
- [83] I. A. Skvortsova, E. D. Orlova, A. O. Boev, D. A. Aksyonov, I. Moiseev, E. M. Pazhetnov, A. A. Savina, and A. M. Abakumov, *J. Power Sources* **583**, 233571 (2023).
- [84] J. E. Huheey, E. A. Keiter, and R. L. Keiter, *Inorganic Chemistry: Principles of Structure and Reactivity* (Harper Collins College, New York, 1993).

- [85] T. Hewston and B. Chamberland, *J. Phys. Chem. Solids* **48**, 97 (1987).
- [86] M. Marezio and J. Remeika, *J. Chem. Phys.* **44**, 3143 (1966).
- [87] T. Ohzuku, A. Ueda, M. Nagayama, Y. Iwakoshi, and H. Komori, *Electrochim. Acta* **38**, 1159 (1993).
- [88] S. Madhavi, G. S. Rao, B. Chowdari, and S. Li, *Electrochim. Acta* **48**, 219 (2002).
- [89] Y. Koyama, Y. Makimura, I. Tanaka, H. Adachi, and T. Ohzuku, *J. Electrochem. Soc.* **151**, A1499 (2004).
- [90] S. Waki, K. Dokko, T. Itoh, M. Nishizawa, T. Abe, and I. Uchida, *J. Solid State Electrochem.* **4**, 205 (2000).
- [91] Y. Sun, Y. Shiosaki, Y. Xia, and H. Noguchi, *J. Power Sources* **159**, 1353 (2006).
- [92] H. Tukamoto and A. West, *J. Electrochem. Soc.* **144**, 3164 (1997).
- [93] M. Reddy, T. W. Jie, C. J. Jafta, K. I. Ozoemena, M. K. Mathe, A. S. Nair, S. S. Peng, M. S. Idris, G. Balakrishna, F. I. Ezema *et al.*, *Electrochim. Acta* **128**, 192 (2014).
- [94] S. Levasseur, M. Ménétrier, and C. Delmas, *Chem. Mater.* **14**, 3584 (2002).
- [95] C. Pouillier, L. Croguennec, P. Biensan, P. Willmann, and C. Delmas, *J. Electrochem. Soc.* **147**, 2061 (2000).
- [96] M. N. Obrovac, O. Mao, and J. R. Dahn, *Solid State Ion.* **112**, 9 (1998).
- [97] J. Yu, Z. Han, X. Hu, H. Zhan, Y. Zhou, and X. Liu, *J. Power Sources* **262**, 136 (2014).
- [98] X. Ma, G. Hautier, A. Jain, R. Doe, and G. Ceder, *J. Electrochem. Soc.* **160**, A279 (2013).
- [99] D. Han, K. Park, J.-H. Park, D.-J. Yun, and Y.-H. Son, *J. Industr. Eng. Chem.* **68**, 180 (2018).
- [100] R. Alcántara, G. Ortiz, J. Tirado, R. Stoyanova, E. Zhecheva, and S. Ivanova, *J. Power Sources* **194**, 494 (2009).
- [101] Y. Wang, T. Cheng, Z.-E. Yu, Y. Lyu, and B. Guo, *J. Alloys Compd.* **842**, 155827 (2020).
- [102] V. Gangadhar, C. Shankaraiah, and G. Prasad, *Transact. Indian Ceram. Soc.* **77**, 26 (2018).
- [103] M. Zou, M. Yoshio, S. Gopukumar, and J.-I. Yamaki, *Chem. Mater.* **15**, 4699 (2003).
- [104] H. Zhang, H. Liu, L. F. Piper, M. S. Whittingham, and G. Zhou, *Chem. Rev.* **122**, 5641 (2022).
- [105] S. S. Zhang, *Energy Stor. Mater.* **24**, 247 (2020).
- [106] Y. Gao, X. Wang, J. Ma, Z. Wang, and L. Chen, *Chem. Mater.* **27**, 3456 (2015).
- [107] A. V. Morozov, I. A. Moiseev, A. A. Savina, A. O. Boev, D. A. Aksyonov, L. Zhang, P. A. Morozova, V. A. Nikitina, E. M. Pazhetnov, E. J. Berg *et al.*, *Chem. Mater.* **34**, 6779 (2022).
- [108] W. Hu, H. Wang, W. Luo, B. Xu, and C. Ouyang, *Solid State Ion.* **347**, 115257 (2020).